International Journal of Hydrogen Energy 136 (2025) 402–412

Contents lists available at ScienceDirect

International Journal of Hydrogen Energy

journal homepage: www.elsevier.com/locate/he

Hydrogen purification from underground storage via pressurized adsorption: Impact of adsorbent properties and operating parameters on methane separation

Selma Kuloglija [a], Neda Asasian Kolur [a,*], Viktor Kalman [a], Christian Jordan [a], Matthias Golda [a], Aleksander Makaruk [b], Ezgi Engin [c], Anton Balla [c], Michael Harasek [a]

[a] Technische Universität Wien, Institute of Chemical, Environmental and Bioscience Engineering, Getreidemarkt 9/166-2, Vienna, 1060, Austria
[b] Axiom Angewandte Prozesstechnik GmbH, Wienerstraße 114, Ebreichsdorf, 2483, Austria
[c] Verbund Green Hydrogen GmbH, Am Hof 6a, Vienna, 1010, Austria

ARTICLE INFO

Keywords:
Hydrogen purification
Pressure swing adsorption
Desorption
Breakthrough modeling
Equilibrium studies

ABSTRACT

This study compared methane adsorption/desorption for hydrogen purification over a pressure range of 1–60 bar at room temperature. The main aim of this work was comparing methane adsorption performance of two commercial activated carbons (GAC and CAC) with different porous properties. GAC, with lower mesoporosity (24 %) and a surface area of 896 m^2/g, demonstrated superior methane capacity and longer breakthrough times at high pressures and low CH_4 concentrations. Conversely, CAC, with higher mesoporosity, exhibited faster adsorption kinetics, especially at lower pressures and higher CH_4 concentrations. The Gompertz model best described dynamic adsorption, while the Bohart-Adams capacity was 0.44 $kmol/m^3$ for CAC and 0.63 $kmol/m^3$ for GAC at 60 bar. Langmuir and BET models showed a maximum monolayer capacity of 4 mmol/g for GAC, with an isosteric heat of 15.48 kJ/mol from the Dubinin-Radushkevich model. Optimal desorption used a H_2 purge-to-feed ratio of 0.16 and 4 bara pressure.

1. Introduction

The energy sector's shift towards addressing climate change and reducing fossil fuel reliance positions hydrogen as a key player in the transition [1,2]. With its high energy content and versatility, hydrogen is crucial for decarbonizing industry and power generation, aligning with global climate goals [3]. However, challenges in hydrogen production and storage remain [4]. The EU views hydrogen as vital for achieving carbon neutrality by 2050 and fulfilling Paris Agreement commitments [5].

Hydrogen can be produced through thermochemical, electrolytic, biological processes, or solar water splitting. Storage options include high-pressure cylinders, cryogenic tanks, adsorption on high surface area materials, absorption in metal interstices, chemical compounds, or reactions with metals like Li, Na, Mg, Al, or Zn [6]. Storing large quantities for medium to long-term use is crucial, particularly as a buffer for seasonal energy fluctuations. A promising method is geological storage in depleted oil and gas reservoirs, aquifers, or caverns in salt, coal, or rock formations [6].

Injecting pure hydrogen into depleted gas reservoirs results in low recovery leads to the need for cushion gas, which maintains pressure and ensures adequate withdrawal rates, contributing to storage costs [7]. These reservoirs still contain natural gas, which acts as cushion gas. When the reservoir is used, methane (CH_4) exits with the hydrogen, making CH_4 the primary impurity that must be removed before hydrogen can be injected into the network [8].

Pressure swing adsorption (PSA) is a cost-effective, energy-efficient technology for separating methane and hydrogen that produces high-purity hydrogen and reduces purification costs [9]. The adaptability of PSA to different feed compositions and conditions makes it suitable for various industrial applications [10]. It operates continuously, can be easily adapted to production requirements and can be seamlessly integrated into existing systems, making it ideal for retrofitting hydrogen plants [11,12]. A wide range of microporous adsorbents can be used, including zeolites, activated carbon and silica gel, with activated carbon often preferred due to its moderate adsorption capacity and efficient desorption properties [13–15].

Yavari et al. compared activated carbon (S_{BET} = 1120 m^2/g) and 5A

* Corresponding author.
E-mail address: neda.asasian@tuwien.ac.at (N. Asasian Kolur).

https://doi.org/10.1016/j.ijhydene.2025.05.090
Received 5 February 2025; Received in revised form 21 April 2025; Accepted 7 May 2025
Available online 10 May 2025

zeolite (S_{BET} = 800 m^2/g) for adsorbing a gas mixture of CO_2, CO, CH_4, and H_2, finding that activated carbon's maximum CH_4 adsorption capacity was 125 % higher due to its larger surface area and diverse pore size [16]. Ribero et al. studied a 4-bed PSA system with layered beds of activated carbon and zeolite, showing that while adding a zeolite layer slightly improved purity and recovery, it eventually limited the effectiveness of the activated carbon in retaining CO_2 [17].

The adsorption and desorption rates of adsorbents are crucial for the efficiency of PSA systems, with materials that have higher contaminant capacity enhancing performance [16,17]. Lopes et al. improved activated carbon's adsorption capacity by altering its microporosity, testing various types, including a commercial one and further activated versions. The modified carbons showed higher adsorption capacities for CO_2, H_2, CH_4, and N_2, with micropore diffusivity increasing by two orders of magnitude compared to the original carbon [18]. He et al. prepared a structured activated carbon adsorbent by dip-coating with a nickel framework to improve mechanical strength. They investigated CO_2 adsorption and CO_2/H_2 separation under different pressures, flow rates and lamella spacing. The structured adsorbent showed a uniform gas flow, a lower pressure drop and sharper breakthrough curves [19].

A review of the literature shows that factors such as adsorbent type, shape, size, structure, specific surface area and microporosity significantly influence CH_4 adsorption capacity. Park et al. developed a highly microporous activated carbon by sacrificial templating of melamine, which was found to be effective for CH_4 and H_2 storage and CH_4/H_2 pressure swing adsorption. This activated carbon with a micropore volume of 1.07 cm^3/g and a specific surface area of 2311 m^2/g showed remarkable CH_4 and H_2 adsorption capacities at 298 K and 70 bar as well as an adsorption capacity of 3.13 mmol/g for CH_4/H_2 separation at a pressure swing of 1–10 bar [20]. Baamran et al. investigated three types of activated carbon with specific surface areas of 990, 2140 and 2480 m^2/g, mesopore volumes of 0.26, 0.96 and 0.89 cm^3/g and micropore volumes of 0.36, 0.65 and 0.83 cm^3/g, respectively. The activated carbon with the highest porosity had the highest CH_4 adsorption capacity [21]. However, the highest H_2 productivity and recovery (99.6 % purity) when separating a multi-component gas mixture ($H_2/CO/CH_4/CO_2$ at 75/5/5/15 by volume) was achieved with the activated carbon with lower porosity and surface area, as it had minimal H_2 equilibrium adsorption capacity despite its lower affinity for other contaminants [21]. In the context of CH_4/H_2 separation, having an excessively large specific surface area and micropore volume in activated carbon is not always beneficial. This is because it can enhance the adsorption capacity for H_2, thereby reducing the efficiency of the PSA process. Additionally, the regeneration of such materials may demand higher energy input, leading to lower selectivity, decreased productivity, and increased energy costs [22].

Therefore, investigating the adsorption behavior of various activated carbons with differing levels of micro and mesoporosity, surface area, and pore size distribution is crucial for the effective separation of CH_4 and H_2. Although some studies have explored methane and hydrogen separation, there remains a critical need for experimental high-pressure data, adsorption breakthrough curves, and equilibrium data. Additionally, there is a noticeable gap in comparative studies that evaluate different types of activated carbon under consistent conditions. Moreover, desorption, a key factor for adsorbent regeneration, has been significantly less studied compared to adsorption.

In this study, the performance of two types of activated carbon with varying surface areas and pore size distributions was compared for methane (CH_4) adsorption under different operating conditions. Adsorption breakthrough curves were utilized to estimate kinetic parameters and adsorption capacities using shortcut models. Key operating parameters, including adsorption pressure, flow rate, and methane inlet concentration, were systematically examined. Equilibrium adsorption data for both activated carbons were obtained and analyzed, showcasing their distinct porous properties. Additionally, the desorption kinetics of CH_4 from saturated activated carbon with the highest adsorption capacity were studied, leading to optimized values for parameters such as the purge-to-feed ratio and desorption pressure.

2. Experimental

2.1. Materials

Two activated carbons were used for the study: (1) CAC: Cylindrical, commercial steam-activated carbon from coconut shells with a 3 mm nominal diameter and 2–8 mm length. It has a bulk density of 457 kg/m^3 and a particle density of 1026 kg/m^3 and (2) GAC: Granular, commercial acid-washed carbon with a 6 × 12 mesh particle size. Its bulk density is 546 kg/m^3, and its particle density is 1221 kg/m^3. The laboratory uses gas cylinders from Messer Austria GmbH, including hydrogen (99.999 %), methane (99.5 %), and helium (99.999 %) for preparing the feed stream.

2.2. Characterization

The adsorbent samples' surface morphology was analyzed with an FEI Quanta FEG-250 SEM. They were mounted on aluminum rods using carbon tape, gold-coated for improved conductivity and reflectance, and then vacuum-coated in a Q150T S sputter coater for 5–10 min at 15 mA. The adsorbents' porous properties were evaluated by N_2 adsorption-desorption at 77 K. Samples were degassed at 350 °C for 8 h. Isotherms provided data on specific surface area, total pore volume and average pore width. Microporosity was assessed using the HK method and mesoporosity using the BJH method [23].

The physical properties of the activated carbons, including density and porosity, were measured as follows: Bulk density (ρ_b) was determined by weighing the adsorbent in a graduated cylinder [24]. Bed porosity (ε_b) was calculated by measuring the volume of water required to fill the voids in the adsorbent-filled cylinder [25]. Particle porosity was estimated from the total pore volume of N_2 adsorption at the highest P/P_0 multiplied by the particle density. Eq. (1) was also used for estimation of particle density. These properties were used to calculate the equilibrium parameters from the dynamic breakthrough data.

$$\epsilon_b = 1 - \frac{\rho_b}{\rho_p} \tag{1}$$

2.3. Adsorption-desorption system

Fig. 1(a) shows a schematic diagram of the gas adsorption-desorption system, including the adsorption column, gas mixture inlet, back pressure control valve, and analysis area. The gas mixture generation system uses precise mass flow controllers (Bronkhorst) to regulate H_2, CH_4, and He (carrier gas). The mixture is fed into an adsorber sub-unit by Axiom angewandte Prozesstechnik GmbH, consisting of a stainless-steel column (SS-316) with a height of 160 cm and an internal diameter of 27.3 mm, designed for operating pressures up to 100 bara [26].

A Swagelok KPB back pressure regulator (SS 316, 0–70 bar inlet and 413 bar outlet) maintains a consistent pressure and ensures continuous flow through the system [27]. Gas flows upward in the adsorber column, with a stainless-steel grid preventing carbon bed fluidization. The adsorber outlet and exhaust lines connect to the gas processing sub-unit and then to the flare for treatment. All experiments are conducted at a stable ambient temperature of 25 °C.

2.4. Methane adsorption-desorption experiments

Methane adsorption-desorption experiments were performed to evaluate activated carbon's ability to adsorb CH_4, separate it from H_2, and allow for regeneration. The adsorption pressure varied from 25 to 60 bara, with feed gas hydrogen content between 70 and 98 v/v%, and the remainder CH_4. As shown in Fig. 1(b), the experiments were divided

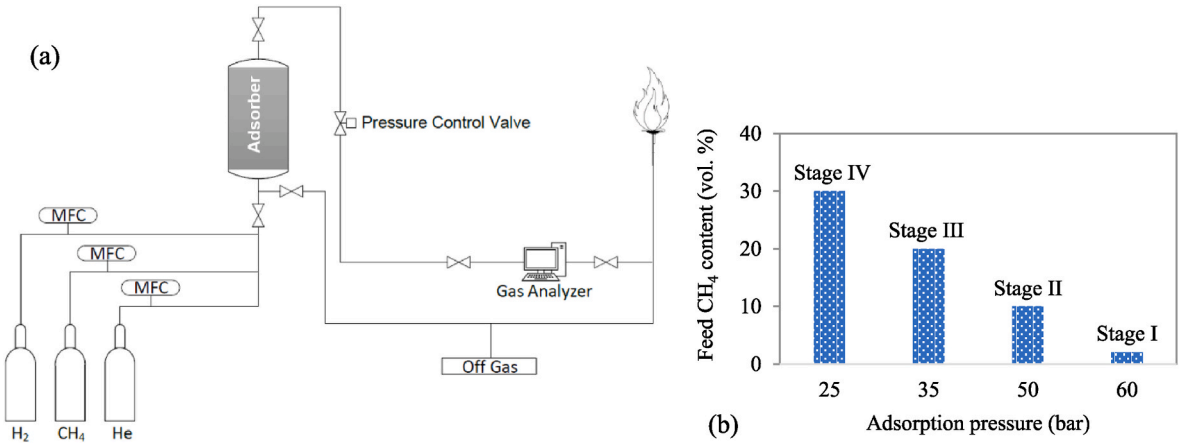

Fig. 1. (a) A schematic of the gas adsorption-desorption system, including the adsorption column, gas mixture inlet, back-pressure control valve, and analysis section, and (b) the operating parameters for different stages of CH_4 breakthrough experiments.

into four stages: Stage I had the highest pressure and lowest methane content, while Stage IV had the lowest pressure and highest methane content. These conditions simulate the transient gas flow from single withdrawals in underground hydrogen storage [27].

Methane concentration in the column outlet was monitored over time during adsorption and desorption, generating breakthrough curves. A SICK GMS810 gas analyzer was used for CH_4/CAC, and an AXIOM speed of sound meter for CH_4/GAC.

Adsorption breakthrough experiments were performed to compare the adsorption capacity of two types of activated carbon under the specified conditions. In further experiments, the effects of total flow rate, adsorption pressure and feed composition were investigated, varying each parameter individually. Some data were used to derive isothermal equilibrium models and parameters as described in section 3.4.

Desorption experiments were conducted by reducing the column pressure via a control valve concurrently and flushing it with pure H_2 at a specific purge ratio. The desorption parameters, including pressure and purge-to-feed ratio, were varied. The purge-to-feed ratio is represented as either the hydrogen in the purge stream to the hydrogen in the feed ($\frac{H_{2,Purge}}{H_{2,Feed}}$) or the total purge flow to the total feed flow (P/F).

All experiments were performed in duplicate for accuracy, and data with less than 95 % accuracy were excluded. Experimental data were fitted to models using MATLAB's curve fitting toolbox. The goodness of fit was assessed using statistical parameters: SSE (Sum of Squared Errors) for total deviation (Eq. (2)), RMSE (Root Mean Square Error) for residual standard deviation (Eq. (3)), and R^2 (Correlation Coefficient) for the proportion of variance explained by the model (Eq. (4)).

$$SSE = \sum_{i=1}^{N} \left(y_{exp,i} - y_{model,i}\right)^2 \tag{2}$$

$$RMSE = \sqrt{\frac{1}{N}\sum_{i=1}^{N} \left(y_{exp,i} - y_{model,i}\right)^2} \tag{3}$$

$$R^2 = 1 - \frac{\sum_{i=1}^{N} \left(y_{exp,i} - y_{model,i}\right)^2}{\sum_{i=1}^{N} \left(y_{exp,i} - \bar{y}_{exp}\right)^2} \tag{4}$$

Where $y_{exp,i}$ is the experimental value, $y_{model,i}$ is the model's predicted value for the ith data point, N the number of data points and $\bar{y}_{exp}$ is the mean of the experimental values.

3. Results and discussion

3.1. Characterization studies

The porous properties of CAC and GAC were characterized using N_2 adsorption-desorption tests at 77 K, with the results summarized in Table 1. CAC exhibited a higher BET specific surface area, larger total pore volume, and greater mesopore volume compared to GAC, while both had similar average pore sizes. The N_2 adsorption-desorption curves in Fig. 2(a) reveal that CAC, with its H_4 hysteresis loop, is classified as a type IV micro-mesoporous adsorbent, indicative of slit-shaped pores [23]. GAC, with a smaller hysteresis loop and a higher microporosity contribution, is classified as type I [23], although it contains a small percentage of mesoporosity.

Fig. 2(b) and (c) depict the pore size distribution of CAC and GAC in the mesopore and micropore regions, respectively. These distributions confirm that CAC has a higher mesopore volume and a lower contribution of micropores compared to GAC. Most mesopores in both carbons have pore sizes below 70 Å. The micropore size distribution shows distinct shapes for the two samples. As shown in Table 1, mesoporosity accounts for approximately 55 % of CAC, while it is less than 25 % in the predominantly microporous GAC.

SEM micrographs in Fig. 2(d) and (e) reveal the morphology and surface texture of CAC and GAC. The GAC surface appears more homogeneous, with uniform pores in shape and size, contributing to consistent adsorption behavior. In contrast, the CAC sample exhibits numerous cracks, fractures, and an inhomogeneous particle distribution, leading to more dispersed mesoporosity. The irregularities in the surface structure of CAC and the more homogeneous structure of GAC influence their respective adsorption capacities.

3.2. Adsorption experiments and modeling

3.2.1. Adsorption breakthrough

The initial adsorption breakthrough experiments compared the adsorption capacities of two activated carbon grades under identical conditions, including pressure and feed composition. Fig. 3 shows breakthrough curves showing the volumetric (molar) CH_4 composition

Table 1
The porous properties of the fresh commercial activated carbons.

Sample	S_{BET} (m^2/g)	V_{tot} (cm^3/g)	$V_{mes,BJH}$ (cm^3/g)	d_{avg} (Å)	Mesoporosity contribution (%)
CAC	1195	0.62	0.34	20.7	55
GAC	896	0.45	0.11	20.1	24

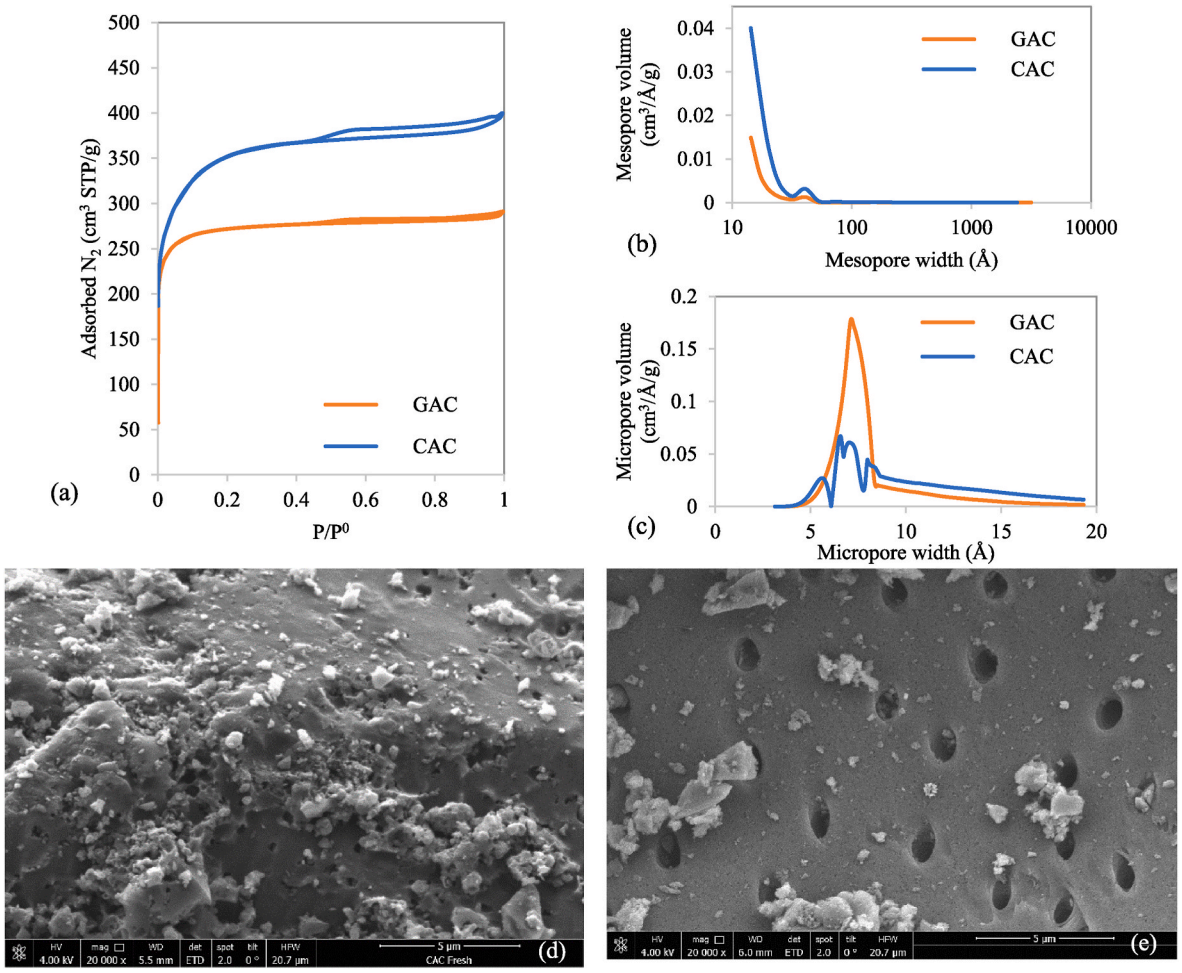

Fig. 2. (a) N_2 adsorption-desorption isotherm curves at 77 K, (b) BJH mesopore size distribution and (c) HK micropore size distribution of fresh commercial activated carbons (GAC and CAC), as well as SEM micrographs of the fresh (d) CAC and (e) GAC samples with the magnification of 20 kx.

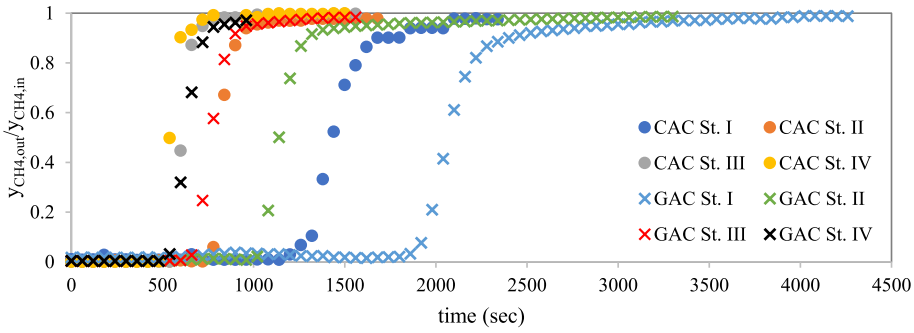

Fig. 3. CH_4 adsorption breakthrough curves at different stages on CAC and GAC activated carbons.

ratio between outlet and inlet, with the curves indicating saturation capacity and mass transfer rates [28]. A comparison of the performances of GAC and CAC shows the superior capabilities of GAC, at high adsorption pressure and when the mole fraction of CH_4 in the feed is low (stages I and II). This superiority is evident from the breakthrough curves, which show a more efficient adsorption process for GAC under these conditions.

Breakthrough times, defined as the duration until the CH_4 outlet-to-inlet ratio reaches 0.05, are shown in Table 2. Both activated carbons exhibit increased breakthrough times from stage IV to stage I due to higher adsorption pressure and lower CH_4 content. For instance, at stage I, GAC maintains CH_4 below 0.001 for about 1890 s, while CAC does so for 1255 s. At stage II, with 50 bar pressure and 0.1 CH_4 concentration, breakthrough times are approximately 1035 s for GAC and 760 s for CAC, indicating the time CH_4 remains below 0.005 at the outlet.

Table 2
Comparison of breakthrough times (sec) for GAC and CAC ($y_{CH4,out}/y_{CH4,in}$ = 0.05 at t_{BT}).

Adsorbents	Stage I	Stage II	Stage III	Stage IV
CAC	1255	760	578	510
GAC	1890	1035	660	545

As adsorption pressure and methane content decrease, the performance difference between GAC and CAC narrows. Lower pressure reduces the driving force for adsorption, leading to shorter breakthrough times. At high pressures and low CH_4 concentrations, micropores dominate adsorption, and GAC's higher microporosity results in longer breakthrough times. In contrast, CAC's higher surface area but greater mesoporosity makes it less effective under these conditions. At lower pressures and higher CH_4 concentrations, adsorption is less influenced by micropores and more by surface area and mesoporosity, reducing the performance gap between GAC and CAC.

This behavior can be further understood by considering the physical mechanisms behind micropore adsorption under these conditions: at high pressures, the gas molecules are more densely packed, increasing the probability of interactions with narrow micropores (<2 nm). These small pores provide high adsorption potentials due to micropore filling by overlapping van der Waals forces from the pore walls, which enhances methane uptake. Meanwhile, under low methane concentrations, the competition among methane molecules for adsorption sites is reduced. In this case, the more energetically favorable sites within micropores dominate the adsorption process. These sites are typically filled first, and because they are more selective, the microporous adsorbent (like GAC) exhibits superior performance in selectively adsorbing methane over hydrogen, which has much lower adsorption affinity. Therefore, the combination of higher pressure (driving force for pore filling) and lower CH_4 concentration (reducing competitive saturation of less selective mesopores) enhances the micropore-driven separation effect.

3.2.2. Breakthrough modeling

This study evaluates several straightforward and reliable models for gas-phase adsorption, including the Bohart-Adams (BA) [29] and Yoon-Nelson (YN) [30] models, both subsets of the logistic model, and the Gompertz model [31], a double exponential model [32]. These models offer parameters that reveal details about adsorbent and adsorbate properties, as well as bed performance.

Table 3 presents the non-linear equations and parameters for the Bohart-Adams (BA), Yoon-Nelson (YN), and Gompertz models, fitted to data from four stages for both adsorption systems. The BA model assumes irreversible adsorption proportional to the residual adsorbent capacity and gas phase concentration, with a rectangular isotherm and homogeneous bed, neglecting axial dispersion [33,34]. The YN model, akin to the logistic equation, provides a probabilistic analysis of breakthrough and predicts symmetrical sigmoidal curves [30]. The Gompertz model, originally for population growth, describes sigmoidal breakthrough curves and effectively handles asymmetric curves [35]. Fig. 4 visually compares the performance of these models in fitting the experimental data.

According to Table 3, all models perform comparably in describing the experimental data, but the Gompertz model slightly outperforms the BA and YN models, as indicated by higher R^2 values and lower SSE and RMSE. This is due to the Gompertz model's ability to handle deviations from the symmetric S-shape of breakthrough curves [38], capturing slight asymmetries effectively. Despite this, the logistic models remain robust for estimating parameters and comparing adsorbent performance.

The BA model parameter, N_0, indicating adsorption capacity per unit volume of the bed, shows that GAC has a higher CH_4 capacity than CAC under the same conditions. Similarly, the Yoon-Nelson parameter, τ_{YN}, representing the time to 50 % breakthrough, confirms GAC's longer breakthrough time compared to CAC, with this difference growing from stage IV to stage I. The ratios of $\frac{N_{0,GAC}}{N_{0,CAC}}$ and $\frac{\tau_{YN,GAC}}{\tau_{YN,CAC}}$ ranging from 1.15 to 1.45, highlight GAC's superior adsorption capacity, especially at higher pressures and lower CH_4 concentrations.

The kinetic comparison of CH_4 adsorption on the two activated

Table 3
Comparative analysis of breakthrough models for the adsorption of CH_4 on CAC and GAC at different stages.[a]

Stage	Adsorbent	Breakthrough models			
		Logistic model $\frac{y_{i,out}}{y_{i,in}} = \frac{1}{1+exp[a-bt]}$	Bohart-Adams $\frac{y_{i,out}}{y_{i,in}} = \frac{1}{1+exp\left[\frac{K_{BA}N_0L}{u} - K_{BA}c_0t\right]}$	Yoon-Nelson $\frac{y_{i,out}}{y_{i,in}} = \frac{1}{1+exp[K_{YN}(\tau_{YN}-t)]}$	Double exponential model; Gompertz [36,37] $\frac{y_{i,out}}{y_{i,in}} = \exp[-\exp(\alpha_G - \beta_G t)]$
I	CAC	a = 17.72	K_{BA} = 0.2525	K_{YN} = 0.0122	α_G = 11.54
		b = 0.0122	N_0 = 0.4413	τ_{YN} = 1448.90	β_G = 0.0083
		R^2 = 0.9938; SSE = 0.2717; RMSE = 0.034			R^2 = 0.9961; SSE = 0.17; RMSE = 0.0269
	GAC	a = 23.78	K_{BA} = 0.2360	K_{YN} = 0.0114	α_G = 15.53
		b = 0.0114	N_0 = 0.6337	τ_{YN} = 2080.49	β_G = 0.0077
		R^2 = 0.9938; SSE = 0.5459; RMSE = 0.0358			R^2 = 0.9953; SSE = 0.4173; RMSE = 0.0313
II	CAC	a = 29.41	K_{BA} = 0.1750	K_{YN} = 0.0353	α_G = 19.49
		b = 0.0353	N_0 = 1.0770	τ_{YN} = 832.67	β_G = 0.0239
		R^2 = 0.9961; SSE = 0.149; RMSE = 0.0297			R^2 = 0.9971; SSE = 0.1105; RMSE = 0.0256
	GAC	a = 21.82	K_{BA} = 0.0941	K_{YN} = 0.0190	α_G = 14.27
		b = 0.0190	N_0 = 1.4862	τ_{YN} = 1149.03	β_G = 0.0128
		R^2 = 0.9958; SSE = 0.2783; RMSE = 0.0290			R^2 = 0.9968; SSE = 0.2124; RMSE = 0.0254
III	CAC	a = 29.19	K_{BA} = 0.1696	K_{YN} = 0.0479	α_G = 19.39
		b = 0.0479	N_0 = 1.3243	τ_{YN} = 609.14	β_G = 0.0326
		R^2 = 0.9969; SSE = 0.1138; RMSE = 0.0260			R^2 = 0.998; SSE = 0.07328; RMSE = 0.0209
	GAC	a = 17.23	K_{BA} = 0.0791	K_{YN} = 0.0223	α_G = 11.27
		b = 0.0223	N_0 = 1.6761	τ_{YN} = 770.92	β_G = 0.0152
		R^2 = 0.9976; SSE = 0.07806; RMSE = 0.0224			R^2 = 0.9988; SSE = 0.04; RMSE = 0.0161
IV	CAC	a = 25.79	K_{BA} = 0.1575	K_{YN} = 0.0477	α_G = 17.11
		b = 0.0477	N_0 = 1.5232	τ_{YN} = 540.90	β_G = 0.0324
		R^2 = 0.9942; SSE = 0.1938; RMSE = 0.0355			R^2 = 0.9957; SSE = 0.1444; RMSE = 0.0306
	GAC	a = 16.39	K_{BA} = 0.0855	K_{YN} = 0.0259	α_G = 10.7
		b = 0.0259	N_0 = 1.7828	τ_{YN} = 633.06	β_G = 0.0176
		R^2 = 0.9970; SSE = 0.05328; RMSE = 0.0234			R^2 = 0.999; SSE = 0.01777; RMSE = 0.0135

[a] a and b: parameters of the logistic equation; K_{BA} (m^3/kmol.s) is the B-A rate coefficient, N_0 (kmol/m^3) is the adsorption capacity of the adsorbent per unit volume of the bed, L (m) is the bed depth, and u (m/s) is the superficial velocity [34]; K_{YN} (1/s) is the Yoon and Nelson rate constant, and τ_{YN} (s) is the time required for reach 50 % adsorbate breakthrough; α_G and β_G (1/s) parameters of the Gompertz equation.

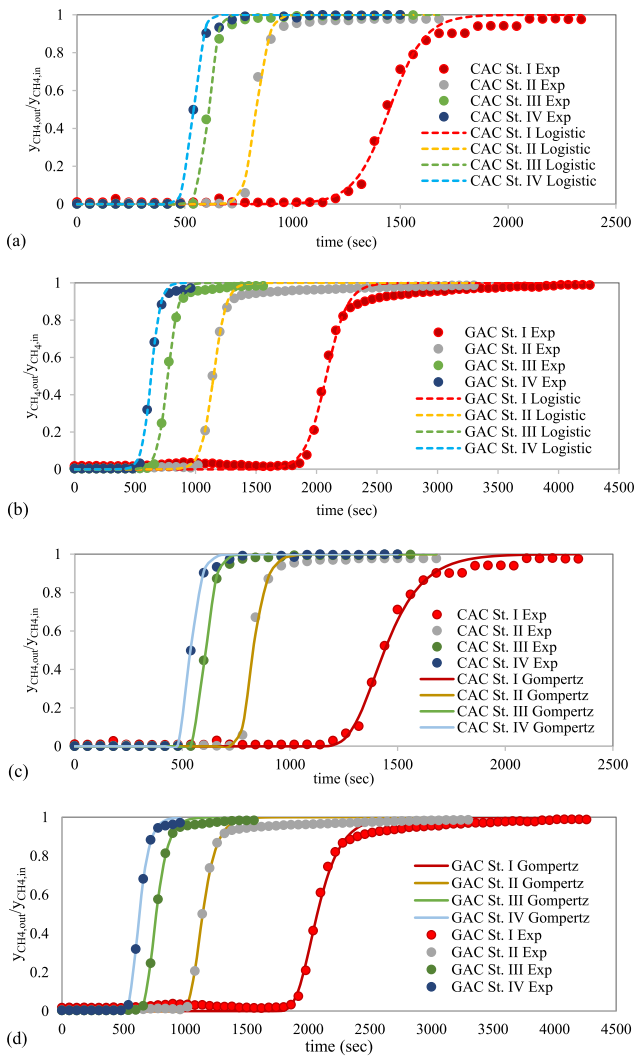

Fig. 4. Breakthrough curves fitted with different models. The curves represent experimental data (dots) and model predictions (dashed lines for the logistic model and line for the Gompertz model).

carbons (GAC and CAC) can be effectively evaluated using several model parameters of these models. A key parameter is the Bohart-Adams rate constant (K_{BA}), which directly relates to the rate at which CH_4 is removed from the gas stream by the adsorbent. Similarly, the Yoon-Nelson rate constant (k_{YN}) reflects the adsorption kinetics and provides information on how fast the adsorption process takes place. A comparison of these parameters shows that CAC has faster adsorption kinetics. Additionally, the Gompertz model shows a higher β_G for CAC, indicating a steeper breakthrough curve. The comparison of kinetic parameters indicates that CAC consistently has a higher adsorption rate than GAC across all stages. Specifically, CAC's rate is nearly twice that of GAC in stages II, III, and IV, and about 1.1 times higher in stage I. This enhanced rate is attributed to CAC's greater mesoporosity, which offers more accessible adsorption sites for CH_4.

This difference in adsorption rates has important implications for the efficiency of hydrogen separation and purification, especially under PSA operation. CAC's higher mesoporosity enables faster CH_4 diffusion, making it more effective for dynamic PSA processes requiring rapid cycles. While GAC offers greater CH_4 and H_2 capacity due to its higher surface area and microporosity, it may also exhibit greater mass transfer resistance, potentially slowing desorption and slightly reducing H_2 recovery.

It is notable that while GAC has higher microporosity, the difference compared to CAC is moderate. CAC's 55 % mesoporosity (vs. 24 % in GAC) supports its faster kinetics. GAC outperforms CAC in CH_4 capacity by 44 % at Stage I, but this advantage drops below 20 % in later stages, indicating that porosity differences may have limited impact on overall performance. Moderate differences in surface area and pore structure lead to modest variations in adsorption/desorption rates. Bohart-Adams parameters show CAC's adsorption rate is up to 2 × faster than GAC's in Stages II–IV and ~10 % faster in Stage I. CAC likely also desorbs faster, though GAC's slower desorption has minimal impact on H_2 recovery.

Ultimately, CAC benefits from faster adsorption and desorption, reduced mass transfer resistance, and shorter cycle times, which can significantly enhance the overall efficiency of H_2 purification—particularly under cyclic or rapid-process conditions where speed and regeneration performance are critical.

3.2.3. Adsorption equilibrium

However, breakthrough models parameters, especially the BA model parameter (N_0), help estimate adsorption equilibrium properties. Additional dynamic adsorption experiments were conducted to derive equilibrium data and isotherm models for granular activated carbon by numerically integrating the breakthrough curves [39,40]. In these experiments, with a constant feed flow rate of 15 L/min, the total pressure ranged from 25 to 60 bar, and CH_4 concentration varied from 0.02 to 0.10. Due to the low CH_4 mole fraction, equal inlet and outlet flow rates were assumed, allowing us to neglect heat of adsorption effects. Under these conditions, H_2 adsorption on activated carbon is negligible [39].

Adsorption loading is calculated using Eq. (5), which measures the CH_4 adsorbed by subtracting the gas-phase CH_4 from the total CH_4 retained by the column during the breakthrough period [40,41].

$$q_{CH_4} = \frac{\frac{P_s}{RT_s}\left(y_{CH4,in}\right)v_f \int_0^{\infty}\left(1-\frac{y_{CH4,out}}{y_{CH4,in}}\right)dt - \frac{P_b}{RT_b}\left(y_{CH4,in}\right)\varepsilon_T V_b}{m} \tag{5}$$

Where q_{CH4} (kmol/kg) is the CH_4 loading of the bed per unit mass of the adsorbent (reported as mmol/g in Table 4), v_f (m^3/s) is the volumetric feed flow rate at standard conditions, P_s (Pa) is the standard pressure, R (Pa.m^3/kmol.K) is the universal gas constant, T_s (K) is the standard temperature, P_b (Pa) is the bed pressure, T_b (K) is the bed temperature, ε_T is the total porosity (calculated from $\varepsilon_T = \varepsilon_b + \varepsilon_p(1-\varepsilon_b)$, where ε_b and ε_p are the bed and particle porosity), V_b (m^3) is the volume of the bed, and m (kg) is the mass of activated carbon in the bed.

Applying Eq. (5) to breakthrough curves at low feed concentrations yields equilibrium data for fitting adsorption models. Eq. (5), based on a constant gas phase volume, calculates the (Gibbs') excess adsorption capacity (q^{exc}_{CH4}) [45,46]. The absolute adsorption capacity (q^{abs}_{CH4}) is then derived by applying a correction term (Eq. (6)) to the excess value before fitting it to isotherms [41]:

$$q_{CH4}{}^{abs} = \frac{q_{CH4}{}^{exc}}{\left(1-\frac{\rho^{gas}_{CH4}}{\rho^{ads}_{CH4}}\right)} \tag{6}$$

The superscripts "abs" and "exc" denote the absolute or excess adsorption capacity, where ρ^{gas} and ρ^{ads} represent the gas phase density of CH_4 [45] and the density of the adsorbed phase [45], respectively. The adsorbed phase density varies with temperature and pressure but generally ranges from 0.30 to 0.40 g/cm^3, with a maximum of 0.421 g/cm^3 at methane's boiling point [46]. For this study, a density of 0.354 g/cm^3 was used [47]. The ideal gas law was suitable for calculating the gas phase density.

Fig. 5 displays the absolute equilibrium adsorption capacity (mmol/g) of CH_4 versus partial pressure (bara). The adsorption equilibrium of CH_4 on GAC is shown in comparison to the results reported for CH_4 adsorption on CAC [26]. The derivation of the CAC isotherm was performed according to the method developed by Malek and Farooq [48].

The experimental CH_4 adsorption data on GAC were initially

Table 4
The parameters of different isotherm models for the adsorption of CH_4 onto GAC.

Langmuir		Dubinin-Radushkevich		Brunauer-Emmet-Teller [42,43,44]	
$q_{CH4}^{abs} = \frac{K_L q_{m,L} P_{CH4}}{1 + K_L P_{CH4}}$		$q_{CH4}^{abs} = q_{0,DR} \exp\left(-K_{DR}\left[RT\ln\left(\frac{\rho^{ads}}{\rho^{gas}}\right)\right]^2\right)$		$q_{CH4}^{abs} = \frac{q_{m,BET} C\left(\frac{\rho^{gas}}{\rho^{ads}}\right)}{\left(1-\frac{\rho^{gas}}{\rho^{ads}}\right)} \frac{\left(1-(n+1)\left(\frac{\rho^{gas}}{\rho^{ads}}\right)^n + n\left(\frac{\rho^{gas}}{\rho^{ads}}\right)^{n+1}\right)}{\left(1+(C-1)\left(\frac{\rho^{gas}}{\rho^{ads}}\right) - C\left(\frac{\rho^{gas}}{\rho^{ads}}\right)^{n+1}\right)}$	
$q_{m,L}$ (mmol/g)	3.9912	$q_{0,DR}$ (mmol/g)	7.034	$q_{m,BET}$ (mmol/g)	3.8981
K_L (1/bara)	0.3886	K_{DR} (mol/kJ)^2	0.0074	n	7.366
R^2	0.9912	R^2	0.9771	C	219.9
RMSE	0.0877	RMSE	0.1224	R^2	0.9870
SSE	0.0923	SSE	0.1648	RMSE	0.0967
				SSE	0.0935

* q_{CH4}^{abs} (mmol/g) is the absolute amount adsorbed, $q_{m,L}$ (mmol/g) is the maximum monolayer adsorption capacity based on Langmuir model, and K_L (1/bara) is the Langmuir equilibrium constant; $q_{0,DR}$ (mmol/g) is the maximum absolute amount of adsorption, limited by the volume filling of the micropores, R (kJ/mol.K) is the gas constant, and T (K) the temperature, ρ^{ads} (kg/m^3) and ρ^{gas} (kg/m^3) are the density of the adsorbed gas and bulk adsorptive gas, K_{DR} (mol/kJ)^2 is an interaction constant related to the characteristic energy of system [43]; $q_{m,BET}$ (mmol/g), represents the maximum monolayer adsorption capacity according to the BET model, C is a constant related to the net heat of adsorption, and n is a parameter representing the number of possible adsorbed layers.

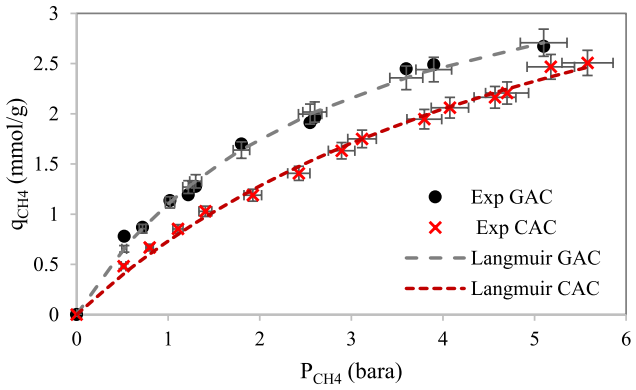

Fig. 5. Isotherm equilibrium data of CH_4 adsorption on CAC and GAC at a temperature of 25 °C, fitted with the Langmuir model.

modeled using the Langmuir isotherm, which assumes monolayer adsorption [49]. Table 4 shows the Langmuir model parameters for CH_4 adsorption on GAC at room temperature, along with statistical data confirming an excellent fit to the experimental equilibrium data. Although the Langmuir model fits the data well, it may not fully capture the physical adsorption mechanism, particularly where multilayer adsorption and pore filling are more likely. Therefore, additional isotherm models were considered to better understand the adsorption mechanism, heat of adsorption, and the number of methane layers formed on the activated carbon surface.

The absolute equilibrium adsorption data were also analyzed using the Dubinin-Radushkevich (DR) isotherm model [50], which is based on pore-filling and Polanyi potential theory, rather than monolayer surface coverage [51]. The original DR equation includes a saturation pressure parameter, but since methane is in a supercritical state at the studied conditions, it lacks a saturation vapor pressure. Therefore, a modified DR equation was used, employing the ratio of ρ^{ads}/ρ^{gas} instead of P_0/P [52]. Table 4 presents the DR model parameters, which fit the data well, though the Langmuir model provided a better fit, indicating that monolayer adsorption may better describe CH_4 adsorption on GAC than pore filling under the range of partial pressure studied.

The DR adsorption isotherm equation can be used to estimate the characteristic energy of the system (E_0) [53], via the equation $E_0 = 1/\left(\sqrt{\beta K_{DR}}\right)$, where β is a similarity coefficient depending only on the adsorptive and for methane the promising value is 0.35 [54]. Dubinin chose benzene as the standard adsorbate for carbonaceous materials (β = 1) because its ring structure resembles the hexagonal carbon arrangement in graphite [55]. Based on the K_{DR} value obtained from the non-linear curve fitting of the DR equation to the CH_4 adsorption experimental data onto GAC, E_0 is calculated to be 19.65 kJ/mol. Additionally, βE_0 can be related to the isosteric heat of adsorption at a fractional filling (∅) of e^{-1} by using the enthalpy of vaporization (ΔH_v) at the boiling point (Eq. (7)) [56,57].

$$q_{st,\varnothing=e^{-1}} = \Delta H_v + \beta E_0 \tag{7}$$

Based on methane enthalpy of vaporization (8.6 kJ/mol) [58], the isosteric heat of adsorption is calculated to be 15.48 kJ/mol. This value is within the range described in the literature for the adsorption of methane on different types of activated carbon [56]. Lopes et al. reported that the isosteric heat of adsorption for CH_4 onto activated carbon, determined using the multisite Langmuir model of Nitta, is 22.7 kJ/mol [57].

The Brunauer-Emmett-Teller (BET) isotherm model, used to study CH_4 adsorption on GAC, extends the Langmuir model by accounting for multiple adsorbed layers while assuming a homogeneous surface and no lateral interactions [59]. The simplified BET equation, typically used for specific surface area (S_{BET}) measurement, assumes an infinite number of layers (Eq. (8)). The general BET equation, with three parameters (Eq. (9)), simplifies to either the Langmuir isotherm or the simplified BET equation depending on the number of adsorbed layers (n) [59]. For gas-phase adsorption at $T > T_c$ [42,44], the undefined saturation pressure (P_0) issue is resolved by substituting P/P_0 with ρ_{gas}/ρ_{ads} [42]. Table 4 presents the non-linear fit parameters of this modified BET equation with the experimental data.

$$q_i = \frac{q_m C P_i}{(P_0 - P_i)\left[1 + \frac{(C-1)P_i}{P_0}\right]} \tag{8}$$

$$q_i = \frac{q_m C\left(\frac{P_i}{P_0}\right)}{\left(1-\frac{P_i}{P_0}\right)} \frac{\left(1-(n+1)\left(\frac{P_i}{P_0}\right)^n + n\left(\frac{P_i}{P_0}\right)^{n+1}\right)}{\left(1+(C-1)\left(\frac{P_i}{P_0}\right) - C\left(\frac{P_i}{P_0}\right)^{n+1}\right)} \tag{9}$$

The $q_{m,BET}$, which represents the maximum adsorption capacity when the entire adsorbent surface is being covered with a complete monomolecular layer [59], agrees well with the value of the corresponding parameter determined with the Langmuir isotherm ($q_{m,L}$). The parameter n, which estimates the number of possible adsorbed layers as about 7. It is notable that this prediction is based on the adsorption in the range of P^0, which was considered in this experiment.

While this section has focused on CH_4 adsorption, the adsorption of hydrogen (H_2) on activated carbon is known to be minimal. Due to the unavailability of a suitable hydrogen detection system in our setup,

direct H_2 adsorption data were not obtained. However, extensive literature reviews support the assumption of negligible H_2 uptake, consistently reporting hydrogen adsorption capacities below 0.5 mmol/g. For example, Choi et al. recorded an H_2 adsorption capacity of 0.36 mmol/g at 293 K and 20 bar [39], while Zhou et al. reported 0.3219 mmol/g at 298 K and 10 bar [37]. Similarly, Siriwardane et al. observed H_2 adsorption values below 0.5 mmol/g even at pressures approaching 20 bar [44,60]. Also, the maximum reported H_2 adsorption capacity reported by Sudibandriyo and Kusumadewi was 0.181 mmol/g at 6.37 bar [61].

Given the consistent trend, assuming negligible H_2 uptake is a reasonable approximation for practical engineering purposes. However, this approach may lack the precision needed for highly sensitive separations, where minor H_2 adsorption could impact performance metrics.

Single-component adsorption measurements using pure gases are the most common and straightforward method for estimating CH_4/H_2 selectivity. Several researchers have reported valuable data on this for activated carbons. Choi et al. measured CH_4 and H_2 isotherms on activated carbon (BET: 1150–1250 m^2/g, pore volume: 0.72 cm^3/g), reporting capacities of 4.25 mmol/g (CH_4) and 0.36 mmol/g (H_2) at 293.15 K and ~20 bar, yielding a CH_4/H_2 selectivity of ~12 under low CH_4 feed conditions [39]. Zhou et al. reported H_2 and CH_4 adsorption on activated carbon (JX101, BET: 1500 m^2/g, pore volume: 0.52 cm^3/g) with capacities of 0.3219 mmol/g (H_2) and 3.7132 mmol/g (CH_4) at 298 K and 10 bar, giving a CH_4/H_2 selectivity of ~12 [37]. Across various studies, CH_4/H_2 selectivity for activated carbons is consistently ~12 at ambient temperatures and 10–20 bar. However, selectivity is higher at lower pressures due to minimal H_2 adsorption; Zhou et al. reported a drop from ~37 at 1 bar to ~12 at 10–20 bar [37]. Furthermore, Mohammad and Sabeeh reported a CH_4/H_2 selectivity of ~5 at 303 K and 30–35 bar [62], reflecting CH_4 saturation at higher pressures, while H_2 adsorption slightly increases, leading to reduced selectivity.

3.2.4. *Effect of operating parameters*

Fig. 6(a–c) illustrates the effects of total flow rate, adsorption pressure, and inlet CH_4 concentration on the adsorption breakthrough curves (BTCs) of CH_4 on GAC. Each parameter is varied independently, while the others are kept constant, to isolate and highlight their specific impacts on the adsorption process.

Fig. 6(a) demonstrates the impact of total inlet flow rate (under standard conditions) on CH_4 adsorption BTCs at a constant adsorption pressure of 50 bar and an inlet CH_4 mole percentage of 10 %. As the flow rate increases, reduced contact time with the adsorbent limits adsorption and hinders effective diffusion of CH_4 molecules to the adsorbent surface. This results in faster saturation of the adsorbent, causing an earlier breakthrough point as the adsorbent reaches its capacity more quickly due to the continuous influx of CH_4 gas, disrupting the dynamic adsorption equilibrium.

Fig. 6(b) shows how varying adsorption pressures (25, 35, and 50 bar) affect the BTCs of CH_4, with a constant inlet concentration of 2 % and a flow rate of 15 L/min. Higher pressures increase gas density and van der Waals forces, enhancing adsorption. This results in a higher capacity and a delayed breakthrough point, as the adsorbent reaches saturation more slowly.

Fig. 6(c) illustrates the effects of varying CH_4 concentrations (2 %, 5 %, and 10 %) on the BTCs, with a constant flow rate of 15 L/min and an adsorption pressure of 50 bar. Higher CH_4 concentrations accelerate saturation as more molecules compete for adsorption sites, leading to an earlier breakthrough. However, the shape and slope of the BTCs' rising part remain consistent, reflecting unchanged adsorption dynamics and mechanisms across different concentrations.

3.3. *Desorption experiments*

The first series of desorption experiments was conducted on a CH_4-saturated GAC column after adsorption breakthrough experiments, based on the conditions explained in Fig. 1(b). Desorption commenced

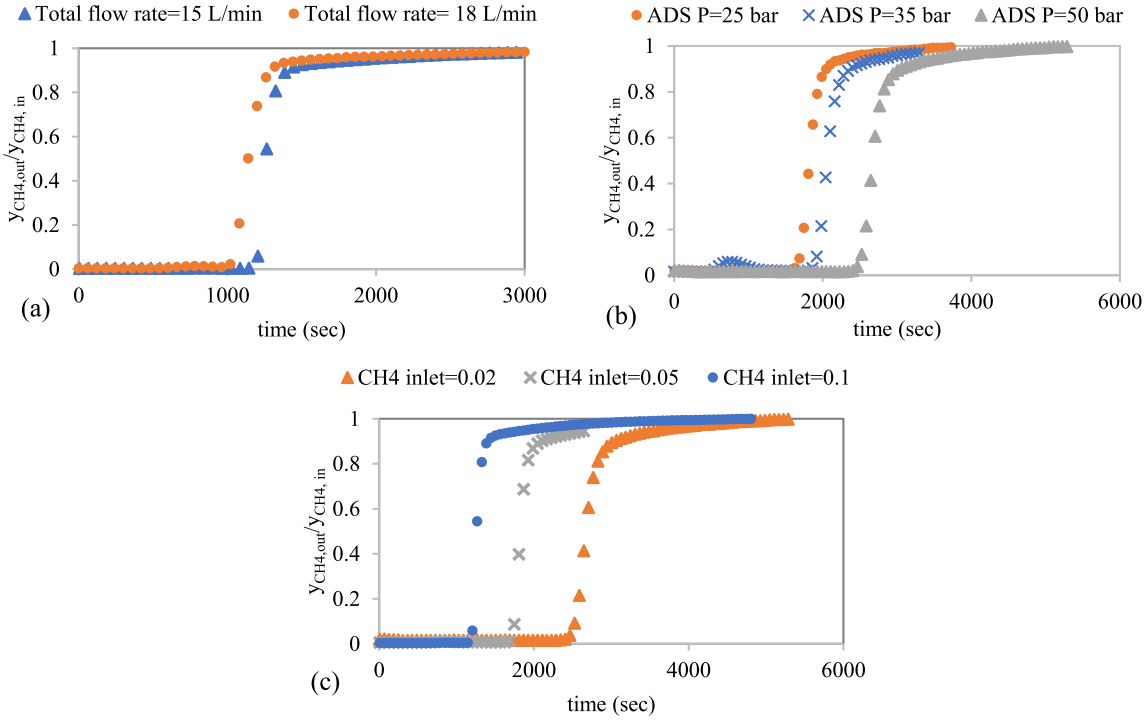

Fig. 6. Breakthrough curves (BTCs) for CH_4 adsorption on GAC under different conditions: (a) effect of total flow rate at a CH_4 feed mole fraction of 0.1 and an adsorption pressure of 50 bar; (b) effect of adsorption pressure at a CH_4 feed mole fraction of 0.02 and a total flow rate of 15 L/min; (c) effect of CH_4 feed mole fraction at an adsorption pressure of 50 bar and a total flow rate of 15 L/min.

once a yCH_4,out/yCH_4, in ratio of 99.5 % was achieved. The time to reach saturation increased with decreasing methane concentration, delaying the start of desorption. The desorption process involved reducing bed pressure to atmospheric levels by co-current gas release while introducing pure H_2 as the purge gas, with a purge-to-feed ratio of 0.25 times the total feed flow. Fig. 7 (a) shows the desorption curves and the corresponding adsorption breakthrough profiles for each stage. The area under the desorption curve, which represents yCH_4, out over time, indicates the amount of desorption. Stage IV has the largest area, reflecting the highest CH_4 adsorption during the adsorption phase under the same conditions.

It is important to note that desorption experiments in this study were conducted solely for GAC. Due to resource constraints, our experimental scope was structured to first compare the two activated carbons based on their adsorption capacities, followed by desorption testing on the carbon (GAC) that exhibited the highest capacity.

3.3.1. *Effect of parameters on desorption kinetics*

Fig. 7 (b) and (c) illustrate the effects of two key parameters on the desorption curves: the $\frac{H_{2,Purge}}{H_{2,Feed}}$ ratio and desorption pressure (P_{des}). The adsorption conditions were consistent across experiments: 50 bar adsorption pressure, 5 % CH_4 inlet composition, and a 10 L/min flow rate. The pressure profile during desorption is indicated by lines in the figures.

Fig. 7 (b) and (c) compare desorption kinetics under varying parameters. Table 5 shows the time required to achieve 95 % desorption at different $\frac{H_{2,Purge}}{H_{2,Feed}}$ ratios and desorption pressures. Increased purge-to-feed ratios and decreased desorption pressures enhance the desorption rate by increasing the driving forces. The most economical $\frac{H_{2,Purge}}{H_{2,Feed}}$ ratio is 0.1, but a small increase to 0.16 is a practical adjustment as it improves desorption kinetics significantly and shortens the time required to achieve the desired desorption. Additionally, desorption at 4 bara shows similar efficiency to atmospheric pressure, making it a viable alternative.

Table 5
Comparison of the time required to achieve 95 % of total desorption under varying parameters.

$\frac{H_{2,Purge}}{H_{2,Feed}}$	Desorption pressure (bara)	Time (sec)
0.10	1	7300
0.16	1	2340
0.26	1	1500
0.53	1	1380
0.10	4.3	7320
0.10	7.6	12120

To further evaluate adsorption–desorption performance, the hydrogen recovery ratio—a critical indicator of PSA system efficiency—was estimated from the simulated adsorption–desorption experiments conducted in this study. The hydrogen recovery ratio is typically defined as the ratio of the moles of H_2 in the product stream to the moles of H_2 in the feed stream, which reflects the efficiency of a PSA

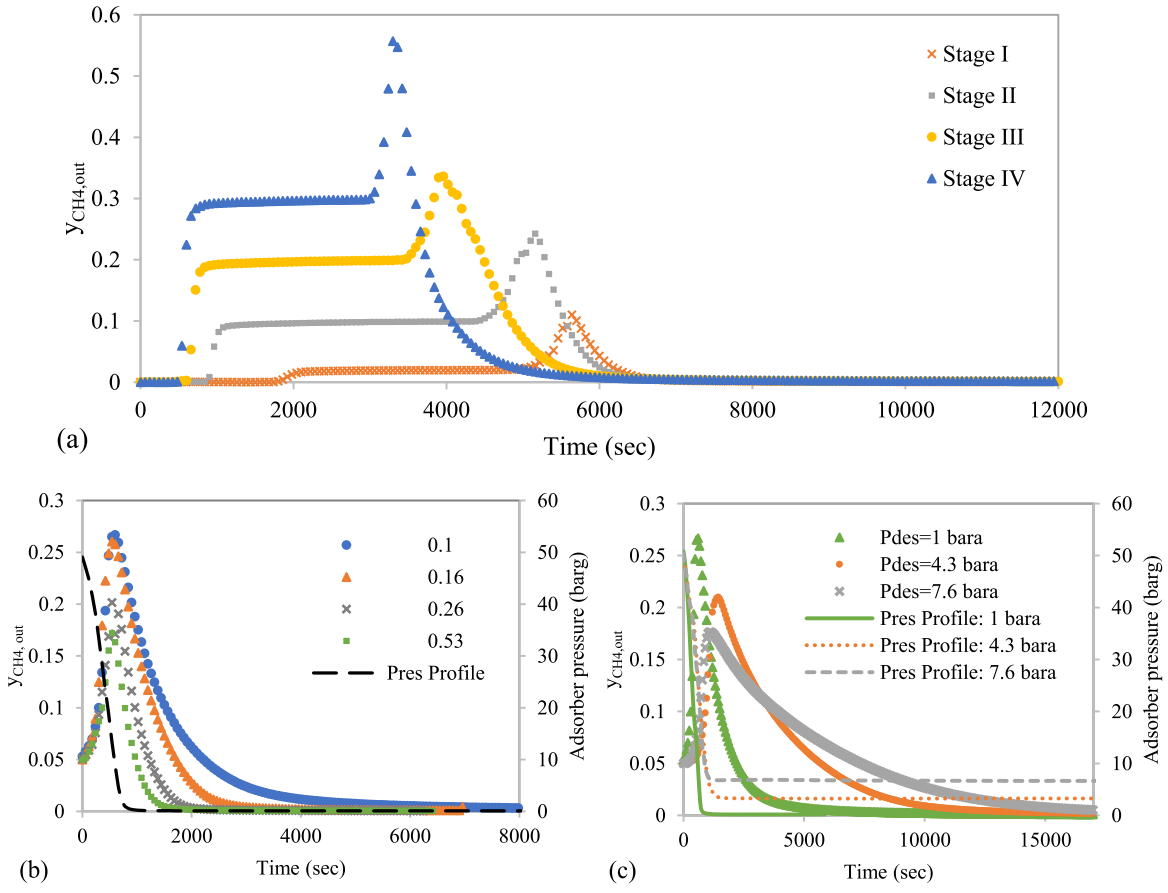

Fig. 7. (a) Breakthrough curves of adsorption at different stages followed by desorption at a total H_2 purge to total feed ratio of 0.25 and a desorption pressure of 1 atm; Effect of (b) $\frac{H_{2,Purge}}{H_{2,Feed}}$ ratio and (c) desorption pressure on the desorption curve of CH_4 from a saturated GAC-filled column. Adsorption conditions: Pressure: 50 bar; $y_{CH4,\ inlet}$: 0.05; Total feed flow: 10 L/min. Desorption was conducted at 1 bara when varying the purge-to-feed ratio, and with a purge-to-feed ratio of 0.1 when varying the desorption pressure.

system in retaining hydrogen while removing impurities. In our study, although full PSA cycle experiments were not conducted, adsorption and desorption tests were performed, an estimation of the hydrogen recovery ratio was made under various test conditions using simplified assumptions—primarily, the negligible adsorption of H_2 on activated carbon.

Adsorption time (t_{ads}) was defined as the period until the outlet CH_4 concentration reached 95 % of the inlet, marking column saturation to calculate the total H_2 fed. During desorption, H_2 purge usage was tracked until 99 % H_2 was observed at the outlet. Assuming negligible H_2 adsorption, recovery was estimated by subtracting purge H_2 from the total H_2 fed. Using this method, H_2 recovery ratios for GAC were approximately 77 %, 58 %, and 40 % for Stages I, II, and III, respectively; Stage IV yielded no reliable result. These relatively low values stem from our experimental setup, which extended adsorption to near-saturation—unlike PSA systems that stop at breakthrough to maximize H_2 recovery.

Additionally, recovery ratios were calculated for experiments investigating the effect of the purge-to-feed ratio. The estimated H_2 recovery values were 83 %, 89 %, 90 %, and 90 % for purge-to-feed H_2 ratios of 0.53, 0.26, 0.16, and 0.10, respectively. It can be observed that a lower purge-to-feed H_2 ratio enhances hydrogen recovery by minimizing purge gas losses; however, it must be carefully optimized to ensure sufficient desorption. The calculated H_2 recovery values quantitatively confirm that a purge-to-feed ratio of 0.16 offers an effective balance between high recovery (90 %) and efficient desorption.

3.4. Application implications based on adsorbent characteristics

The comparative analysis of GAC and CAC behaviors enables the determination of each material's suitability for specific applications. CAC's higher mesoporosity promotes faster desorption kinetics, allowing quicker release of adsorbed methane. This trait is especially beneficial in processes requiring frequent adsorbent regeneration, as it minimizes downtime and boosts overall PSA efficiency—making CAC well-suited for high-frequency cycling operations. CAC's faster adsorption kinetics make it ideal for applications requiring rapid gas uptake, such as systems with variable feed composition or high throughput. Suitable examples include dynamic gas separation, high-flow processes, and emergency response scenarios requiring swift contaminant removal.

GAC's higher microporosity may lead to slower desorption kinetics compared to CAC, resulting in a more gradual release of adsorbed methane. This controlled desorption supports a stable and continuous flow of purified hydrogen, making GAC well-suited for applications that demand consistent output and high gas purity. With its higher adsorption capacity, GAC is ideal for applications focused on maximizing gas capture under stable feed conditions. Key examples include long-term gas storage, high-purity gas production, and buffer systems for managing seasonal energy fluctuations through hydrogen storage and release.

4. Conclusions

This study examined methane adsorption on two types of activated carbon (CAC and GAC) up to 60 bara. GAC, with its primarily microporous structure, demonstrated superior methane capacity, especially at high pressures and low concentrations. Breakthrough curves were modeled using both logistic and double exponential models, with the latter providing a better fit for asymmetric curves. CAC, featuring higher mesoporosity, showed faster adsorption kinetics. Langmuir modeling effectively described GAC adsorption up to 6 bar, while BET modeling suggested approximately seven adsorbed layers. The DR model yielded an isosteric heat of adsorption of 15.48 kJ/mol, consistent with literature values. Increased flow rate and CH_4 concentration led to earlier saturation and breakthrough, while higher pressure delayed breakthrough. Desorption efficiency improved with a H_2 purge-to-feed ratio of 0.16 and a desorption pressure of 4 bara, which was sufficiently low for effective methane separation. In conclusion, GAC is best for high capacity, while CAC excels in kinetics, allowing for optimization based on specific application requirements.

CRediT authorship contribution statement

Selma Kuloglija: Writing – original draft, Methodology, Investigation. **Neda Asasian Kolur:** Writing – review & editing, Methodology, Formal analysis, Data curation. **Viktor Kalman:** Methodology, Data curation. **Christian Jordan:** Software, Methodology. **Matthias Golda:** Methodology. **Aleksander Makaruk:** Validation, Formal analysis, Conceptualization. **Ezgi Engin:** Resources, Project administration, Conceptualization. **Anton Balla:** Resources, Project administration, Conceptualization. **Michael Harasek:** Supervision, Resources, Project administration, Funding acquisition, Conceptualization.

Funding

This research was partially supported by the Österreichische Forschungsförderungsgesellschaft FFG within the research project "Underground Sun Storage 2030 (USS2030)" (FFG Project # 880764).

Declaration of competing interest

The authors declare that they have no known competing financial interests or personal relationships that could have appeared to influence the work reported in this paper.

Acknowledgments

The authors gratefully acknowledge the financial support provided by TU Wien Bibliothek through its Open Access Funding Programme. They also extend their sincere thanks to Axiom Angewandte Prozesstechnik GmbH for generously supplying the speed of sound measuring device, and some other equipment used in this research. Additionally, the authors would like to thank the Forschungsgruppe Technische Katalyse, TU Wien, for their assistance in measuring the porous properties.

References

[1] Hassan Q, Algburi S, Sameen AZ, Salman HM, Jaszczur M. Green hydrogen: a pathway to a sustainable energy future. Int J Hydrogen Energy 2024;50:310–33.
[2] Bermudez JM, Evangelopoulou S, Pavan F. Tracking hydrogen IEA [Online]. Available: https://www.iea.org/energy-system/low-emission-fuels/hydrogen. [Accessed 22 August 2024].
[3] Hassan Q, Sameen AZ, Salman HM, Jaszczur M, Al-Jiboory AK. Hydrogen energy future: advancements in storage technologies and implications for sustainability. J Energy Storage 2023;72:108404.
[4] Ajanovic A, Sayer M, Haas R. The economics and the environmental benignity of different colors of hydrogen. Int J Hydrogen Energy 2022;47(57):24136–54.
[5] Jahanbakhsh A, Potapov-Crighton AL, Mosallanezhad A, Kaloorazi NT, Maroto-Valer MM. Underground hydrogen storage: a UK perspective. Renew Sustain Energy Rev 2024;189:114001.
[6] Zivar D, Kumar S, Foroozesh J. Underground hydrogen storage: a comprehensive review. Int J Hydrogen Energy 2021;46(45):23436–62.
[7] Zamehrian M, Sedaee B. Underground hydrogen storage in a partially depleted gas condensate reservoir: influence of cushion gas. J Pet Sci Eng 2022;212:110304.
[8] Kalman V, Makaruk A, Engin E, Balla A, Harasek M. Simulation of hydrogen-methane separation with pressure swing adsorption. In: Computer aided chemical engineering, vol. 53. Elsevier; 2024. p. 931–6.
[9] Abd AA, Othman MR, Naji SZ, Hashim AS. Methane enrichment in biogas mixture using pressure swing adsorption: process fundamental and design parameters. Mater Today Sustain 2021;11:100063.
[10] Grande CA. Advances in pressure swing adsorption for gas separation. Int Sch Res Not 2012;2012(1):982934.
[11] Burgers I, Dehdari L, Xiao P, Li KG, Goetheer E, Webley P. Techno-economic analysis of PSA separation for hydrogen/natural gas mixtures at hydrogen refuelling stations. Int J Hydrogen Energy 2022;47(85):36163–74.
[12] Li C, et al. Multi-objective optimization of breakthrough times for hydrogen purification through layered bed pressure swing adsorption based on genetic

algorithm and artificial neural network model. Int J Hydrogen Energy 2024;52:390–405.
[13] Sircar S, Golden TC, Rao MB. Activated carbon for gas separation and storage. Carbon N Y 1996;34(1):1–12.
[14] Py X, Goetz V, Plantard G. Activated carbons textural optimization for gas storage processes. Chem Eng Process Process Intensif 2008;47(3):308–15.
[15] Luberti M, Ahn H. Review of Polybed pressure swing adsorption for hydrogen purification. Int J Hydrogen Energy 2022;47(20):10911–33.
[16] Yavary M, Ale Ebrahim H, Falamaki C. Competitive adsorption equilibrium isotherms of CO, CO2, CH4, and H2 on activated carbon and zeolite 5A for hydrogen purification. J Chem Eng Data 2016;61(10):3420–7.
[17] Ribeiro AM, Grande CA, Lopes FVS, Loureiro JM, Rodrigues AE. A parametric study of layered bed PSA for hydrogen purification. Chem Eng Sci 2008;63(21):5258–73.
[18] Lopes FVS, Grande CA, Ribeiro AM, Oliveira ELG, Loureiro JM, Rodrigues AE. Enhancing capacity of activated carbons for hydrogen purification. Ind Eng Chem Res 2009;48(8):3978–90.
[19] He B, Liu J, Zhang Y, Zhang S, Wang P, Xu H. Comparison of structured activated carbon and traditional adsorbents for purification of H2. Sep Purif Technol 2020;239:116529.
[20] Park Y-J, Choi HL, Bae T-H. Highly microporous activated carbons synthesized from sacrificial templating of melamine for CH4 and H2 storages and CH4/H2 adsorptive separation. Fuel 2024;377:132765.
[21] Baamran K, Al-Naddaf Q, Lawson S, Rownaghi AA, Rezaei F. Kinetic process assessment of H2 purification over highly porous carbon sorbents under multicomponent feed conditions. Sep Purif Technol 2023;306:122695.
[22] Silva B, et al. H2 purification by pressure swing adsorption using CuBTC. Sep Purif Technol 2013;118:744–56.
[23] Sing KSW. Reporting physisorption data for gas/solid systems with special reference to the determination of surface area and porosity (Recommendations 1984). Pure Appl Chem 1985;57(4):603–19.
[24] Index C. 258⟨ 616⟩ Bulk Density and Tapped Density of Powders/Physical Tests USP 35. 2011.
[25] Worch E. Adsorption technology in water treatment, vol. 10. Berlin: de Gruyter; 2012.
[26] Kalman V, Voigt J, Jordan C, Harasek M. Hydrogen purification by pressure swing adsorption: high-pressure PSA performance in recovery from seasonal storage. Sustainability 2022;14(21):14037.
[27] Voigt J. Pressure Swing Adsorption for the Purification of Hydrogen from Porous Storage Reservoirs. Vienna: TU Wien; 2022.
[28] Wang S, Huang L, Zhang Y, Li L, Lu X. A mini-review on the modeling of volatile organic compound adsorption in activated carbons: equilibrium, dynamics, and heat effects. Chin J Chem Eng 2021;31:153–63.
[29] Bohart GS, Adams EQ. Some aspects of the behavior of charcoal with respect to CHLORINE.1. J Am Chem Soc Mar. 1920;42(3):523–44. https://doi.org/10.1021/ja01448a018.
[30] Yoon YH, Nelson JH. Application of gas adsorption kinetics I. A theoretical model for respirator cartridge service life. Am Ind Hyg Assoc J 1984;45(8):509–16.
[31] Gompertz B. On the nature of the function expressive of the law of human mortality, and on a new mode of determining the value of life contingencies. In a letter to Francis Baily, Esq. FRS &c. By Benjamin Gompertz, Esq. FR S. In: Abstracts of the papers printed in the philosophical transactions of the royal society of london. The Royal Society London; 1833. p. 252–3.
[32] Hu Q, Xie Y, Feng C, Zhang Z. Prediction of breakthrough behaviors using logistic, hyperbolic tangent and double exponential models in the fixed-bed column. Sep Purif Technol 2019;212:572–9.
[33] Lau LC, MohamadNor N, Lee KT, Mohamed AR. Adsorption isotherm, kinetic, thermodynamic and breakthrough curve models of H2S removal using CeO2/NaOH/PSAC. Int J Petrochem Sci Eng 2016;1(2):36–44.
[34] Chu KH. Breakthrough curve analysis by simplistic models of fixed bed adsorption: in defense of the century-old Bohart-Adams model. Chem Eng J 2020;380:122513.
[35] Banisheikholeslami A, Qaderi F. A novel machine learning framework for predicting biogas desulfurization breakthrough curves in a fixed bed adsorption column. Bioresour Technol Rep 2024;25:101702. https://doi.org/10.1016/j.biteb.2023.101702.
[36] Belmabkhout Y, Frere M, De Weireld G. High-pressure adsorption measurements. A comparative study of the volumetric and gravimetric methods. Meas Sci Technol 2004;15(5):848.
[37] Wu Q, Zhou L, Wu J, Zhou Y. Adsorption equilibrium of the mixture CH4+ N2+ H2 on activated carbon. J Chem Eng Data 2005;50(2):635–42.
[38] Chu KH. Fitting the Gompertz equation to asymmetric breakthrough curves. J Environ Chem Eng 2020;8(3):103713.
[39] Choi B-U, Choi D-K, Lee Y-W, Lee B-K, Kim S-H. Adsorption equilibria of methane, ethane, ethylene, nitrogen, and hydrogen onto activated carbon. J Chem Eng Data 2003;48(3):603–7.
[40] Becnel JM, Holland CE, McIntyre J, Matthews MA, Ritter JA. Fundamentals of fixed bed adsorption processes: analysis of adsorption breakthrough and desorption elution curves. In: American society for engineering education annual conference & exposition; 2002. Citeseer.
[41] Aji AQM, Mohshim DF, Maulianda B, Elraeis KA. Supercritical methane adsorption measurement on shale using the isotherm modelling aspect. RSC Adv 2022;12(32):20530–43.
[42] Zhou S, Zhang D, Wang H, Li X. A modified BET equation to investigate supercritical methane adsorption mechanisms in shale. Mar Petrol Geol 2019;105:284–92.
[43] Rexer TFT, Benham MJ, Aplin AC, Thomas KM. Methane adsorption on shale under simulated geological temperature and pressure conditions. Energy & Fuels 2013;27(6):3099–109.
[44] Siriwardane RV, Shen MS, Fisher EP, Poston JA. Adsorption of CO2 on molecular sieves and activated carbon. Energy & Fuels 2001;15(2):279–84.
[45] Myers AL, Monson PA. Adsorption in porous materials at high pressure: theory and experiment. Langmuir 2002;18(26):10261–73.
[46] Chen L, Liu K, Jiang S, Huang H, Tan J, Zuo L. Effect of adsorbed phase density on the correction of methane excess adsorption to absolute adsorption in shale. Chem Eng J 2021;420:127678.
[47] Saleman T, Xiao G, Li G, May EF. A robust dynamic column breakthrough technique for high-pressure measurements of adsorption equilibria and kinetics. Adsorption 2017;23:671–84.
[48] Malek A, Farooq S. Hydrogen purification from refinery fuel gas by pressure swing adsorption. AIChE J 1998;44(9):1985–92.
[49] Langmuir I. The adsorption of gases on plane surfaces of glass, mica and platinum. J Am Chem Soc 1918;40(9):1361–403.
[50] Hutson ND, Yang RT. Theoretical basis for the Dubinin-Radushkevitch (DR) adsorption isotherm equation. Adsorption 1997;3:189–95.
[51] Sakurovs R, Day S, Weir S, Duffy G. Application of a modified Dubinin–Radushkevich equation to adsorption of gases by coals under supercritical conditions. Energy & fuels 2007;21(2):992–7.
[52] Chen L, et al. Application of Langmuir and Dubinin–Radushkevich models to estimate methane sorption capacity on two shale samples from the Upper Triassic Chang 7 Member in the southeastern Ordos Basin, China. Energy Explor Exploit 2017;35(1):122–44.
[53] Stoeckli F. Dubinin" s theory and its contribution to adsorption science. Russ Chem Bull 2001;50(12):2265–72.
[54] Wood GO. Activated carbon adsorption capacities for vapors. Carbon N Y 1992;30(4):593–9.
[55] Nguyen C, Do DD. The Dubinin–Radushkevich equation and the underlying microscopic adsorption description. Carbon N Y 2001;39(9):1327–36.
[56] Abdulsalam J, Mulopo J, Bada SO, Oboirien B. Equilibria and isosteric heat of adsorption of methane on activated carbons derived from South African coal discards. ACS Omega 2020;5(50):32530–9.
[57] Lopes FVS, et al. Adsorption of H2, CO2, CH4, CO, N2 and H2O in activated carbon and zeolite for hydrogen production. Separ Sci Technol 2009;44(5):1045–73.
[58] Ott JB, Goates JR, Lamb JD. Solid-liquid phase equilibria in water+ ethylene glycol. J Chem Thermodyn 1972;4(1):123–6.
[59] Yu W, Sepehrnoori K, Patzek TW. Modeling gas adsorption in Marcellus shale with Langmuir and bet isotherms. SPE J 2016;21(2):589–600.
[60] Siriwardane R, Shen M, Fisher E, Poston J, Shamsi A. Adsorption and desorption of CO2 on solid sorbents (No. DOE/NETL-2001/1144). National Energy Technology Laboratory, and Morgantown, WV (United States); 2001.
[61] Sudibandriyo M, Kusumadewi F. Hydrogen recovery from hydrogen-methane gas mixture using coffee grounds based activated carbon bioadsorbent. In: E3S Web of Conferences, vol. 67. EDP Sciences; 2018, 02046.
[62] Abbas Khalaf M, Shareef Sabeeh N. Comparative study for adsorption of hydrogen-methane mixtures on activated carbon and 5A molecular sieve. Braz J Chem Eng 2018;35(2):795–804.